Desalination and Water Treatment
www.deswater.com

doi: 10.5004/dwt.2020.24910

177 (2020) 186–196
February

Facile synthesis of Zn-doped $Bi(OH)_3$ with upward surface band bending and its enhanced visible light photocatalytic activity

Xiaoxing Zeng[a,b], Zhaodi Xu[c,*], Xiaofeng Gong[a,*], Yiqun Wan[c]

[a]*School of Resource Environmental and Chemical Engineering, Nanchang University, Nanchang 330031, China, email: xfgong@ncu.edu.cn (X. Gong)*
[b]*Institute of Photovoltaics, Nanchang University, Nanchang, 330031, China*
[c]*Center of Analysis and Testing, Nanchang University, Nanchang 330047, China, email: xuzhaodi@ncu.edu.cn*

Received 2 April 2019; Accepted 16 September 2019

ABSTRACT

In this study, $Bi(OH)_3$ doped with different contents of zinc were successfully prepared via a facile solvothermal approach and characterized by various characterization technologies. The photocatalytic performance of the obtained samples was evaluated by degradation of Rhodamine B (RhB) under visible light irradiation ($\lambda \geq 420$ nm). The results revealed that Zn doping changed the energy band structure of the catalysts and caused upward band bending. Accordingly, the adsorption capability of the catalysts was enhanced. The transfer rate of photogenerated carriers was improved and the recombination of carriers was inhibited. When the optimum Zn/Bi molar ratio was 0.02, the reaction rate constant of the obtained sample was as 5.0 times high as that of pure $Bi(OH)_3$. Active species experiments demonstrated that photogenerated holes played the key role for degradation of RhB. The possible carriers transfer route was discussed on the basis of the experiment results.

Keywords: $Bi(OH)_3$; Zinc; Photocatalytic activity; Rhodamine B (RhB); Upward band bending

1. Introduction

Effluent containing large amounts of dyes can pose a threat to aquatic life and endanger human health. Accordingly, the treatment for dye wastewaters was the growing needs of the present time [1–3]. Semiconductor photocatalysis as a "green" technology has been widely applied for decomposing environmental pollutants especially for the wastewater [4,5]. It is well known that catalyst is the most important part of the photocatalytic technology. Therefore, the exploitation and preparation of new efficient photocatalysts have become a hot topic in current photocatalytic research. Bismuth hydroxide ($Bi(OH)_3$) is the less studied semiconductor material of the containing bismuth compounds. Zhang et al. [6] reported $Bi(OH)_3$ nanoflakes as the pseudocapacitor material and there are no reports about single-phase $Bi(OH)_3$ catalyst applied for photocatalytic degradation of pollutants. As we all known, single-phase catalyst has usually the disadvantages of quick recombination of the photogenerated electron–hole pairs in the process of photocatalytic reaction, which limits its practical application [7,8]. Up to now, numerous techniques have been employed to enhance the photocatalytic efficiency, such as deposition of noble metals [9], ion doping or coupled with metal oxide [10] and co-catalysts [11,12]. Among these, ion doping is a simple and much more research way. Pare et al. [13] reported that manganese-doped BiOCl showed an enhanced photocatalytic activity for degradation of malachite green dye. It was proved that Mn doping enabled the catalyst to absorb more visible light due to absorption edge shift toward higher wavelength. Additionally Mn^{2+} ions by scavenging electrons increase life time of photogenerated electrons and holes. Li et al. [14] reported that Zn doping could promote

* Corresponding authors.

the separation of photogenerated electron–hole pairs of the catalyst and improve the specific surface area comparing with the pure BiOCl. Song et al. [15] reported that Zn-doped BiOBr hierarchical nanostructures exhibited excellent visible light activity for the degradation of RhB. The excellent photocatalytic activity of the Zn-doped BiOBr ascribed to the Zn dopant acting as the holes traps, which suppressed the recombination of the electrons and holes.

The difference of density of electrons between the bulk and surface of the semiconductor may induce surface band bending [16,17]. Doping ions with different numbers of charges substituting metal ions in semiconductors may result in the formation of space electric field, which could change the energy band edges in the semiconductor [18–21]. Since the band positions were closely related to the surface physical and chemical properties of the semiconductors [22–24], the surface band bending and the associated electric field in the space charge region can not only promote the separation of electrons and holes but also influence the thermal adsorption or desorption of reactant on surface of the catalyst [25–28].

In the present study, band bending and band potential shifts were identified at the surface of the Zn-doped $Bi(OH)_3$ catalysts. Accordingly, the photocatalytic degradation for RhB of the obtained catalysts was investigated. The interaction between the semiconductors and the attached RhB was discussed. This interaction may be important with regard to understanding and controlling photogenerated carriers transfer due to carriers transfer rate depending on the energy band edges and interfacial electric fields.

2. Experimental

2.1. Preparation of photocatalysts

All the chemicals were of analytical purity and used without further purification. The preparation procedure was modified on the basis of the literature [6]. Typically, 2 mmoL $Bi(NO_3)_3{\cdot}5H_2O$ and different amounts of $Zn(NO_3)_2{\cdot}6H_2O$ with a Zn/Bi molar ratio (denoted as *R*) of 0, 0.01, 0.02, 0.03 and 0.04 were dissolved in 50 mL ethylene glycol (EG) with strong stirring, respectively. Then another 20 mL H_2O solution containing 2 mmoL $CH_3COONa{\cdot}3H_2O$ was dropped into the above solution under continuous stirring. After continuous stirring for 0.5 h, the resulting suspension was transferred into a 100 mL Teflon-lined stainless autoclave and maintained at 180°C for 12 h. After cooling down to room temperature naturally, the precipitate was washed with absolute ethanol and distilled water several times, and dried at 60°C in air. The obtained samples were denoted as BOH and BOH-Zn*R* (*R* = 0.01, 0.02, 0.03 and 0.04).

2.2. Characterization

XRD patterns were acquired with a Bruker D8 advance X-ray diffractometer employing Cu Ka (λ = 1.5418 Å) radiation. The voltage and current were 40 kV and 40 mA, respectively. Scanning electron microscopy (SEM) images were taken with a JSM 6701F field emission scanning electron microscope. Transmission electron microscopy (TEM) images were taken using a JEM-2100 field emission transmission electron microscope working at 200 kV. UV–Vis diffuse reflectance spectra were obtained using a TU-1900 spectrophotometer using $BaSO_4$ as a reference and were converted from reflection to absorbance via the Kubelka–Munk method. UV–Vis absorption spectra were obtained using a Shimadzu UV-2501PC spectrophotometer. Fluorescence emission spectra (PL) were recorded using a Hitachi F-4500 type fluorescence spectrophotometer with a 360 nm excitation source over a wavelength range of 400–600 nm. X-ray photoelectron spectroscopy (XPS) spectra using an Al Kα X-ray source with 1,486.6 eV energy were performed on a Thermo Scientific Escalab 250Xi and the binding energy was calibrated against C1s (284.8 eV). Fourier transform infrared spectra (FTIR) were recorded at room temperature with a KBr pellet on Nicolet 5700 spectrometer. The specific surface areas and nitrogen adsorption–desorption curves of the samples were determined using a JW-BK132F analyzer. Before the nitrogen adsorption–desorption analysis, the samples were heated and dehydrated for 2 h at 110°C and under N_2 atmosphere.

2.3. Photocatalytic activity

The photocatalytic activity of the prepared samples was evaluated via degradation of RhB aqueous solution under visible light irradiation ($\lambda \geq 420$ nm). A 300 W Xe lamp with 420 nm cut off filter was used as the light source. 500 mL of quartz photoreactor was equipped with a magnetic bar and a water circulating jacket. In a typical photocatalytic experiment, 0.10 g of the as-prepared catalysts were added to 250 mL of RhB aqueous solution (10 mg L^{-1}). The suspension was treated via ultrasonication and then magnetic stirring in the dark for 40 min to reach an adsorption–desorption equilibrium between the photocatalyst and RhB before irradiation. Subsequently, at intervals of every 20 min, about 4 mL of suspension was sampled and separated via the filter membrane of a syringe to remove the catalyst particles. The absorbance of the solution was analyzed via using a UV–Vis spectrophotometer. The degradation efficiency of target pollutant (RhB) was calculated by the following equation:

$$\text{Removal} = \left(1 - \frac{C}{C_0}\right) \times 100\% \quad (1)$$

where C_0 is the concentration of RhB after adsorption–desorption equilibrium, C is the residual concentration of RhB at different illumination intervals.

2.4. Detection of reactive species

Isopropanol (IPA) and triethanolamine (TEOA) were the quencher of hydroxyl radicals ($^{\bullet}OH$) and holes (h^+) under light illumination, respectively. In order to detect the active species during photocatalytic reaction, photocatalytic efficiency of the samples was investigated via further adding 1.0 mmol L^{-1} IPA and 1.0 mmoL L^{-1} TEOA solution into the photoreaction suspension, respectively. Additionally, nitroblue tetrazolium (NBT, 2.5 × 10^{-5} moL L^{-1}, exhibiting an absorption maximum at 259 nm) was used to determine the amount of superoxide radical ($O_2^{\bullet -}$) generated from the

photocatalysts. The method was similar to the former photocatalytic activity test only replacing the RhB solution with NBT solution.

3. Results and discussion

3.1. Crystallographic study

Fig. 1 shows the XRD patterns of all the samples. All the diffraction peaks are matched well with the standard pattern for $Bi(OH)_3$ (JCPDS: 01-0898) and no other diffraction peaks could be observed, indicating that Zn doping do not change the phase composition. However, it is worth noting that the peak intensities of BOH-Zn become weaker with increase of the zinc content (Fig. 1a), indicating the reduction in crystallization of the obtained samples. Further observation of diffraction peaks in the range of 20°–35° is shown in Fig. 1b. The peak positions of BOH-Zn shift towards the higher angle with increase of the zinc concentrations. Based on the Bragg equation: $d(hkl) = \lambda/(2\sin\theta)$, the diffraction peaks shifting to the higher angles result in the decrease in interplanar distance (d). As the ionic radius of Zn^{2+} (0.074 nm) is smaller than that of Bi^{3+} (0.103 nm) [14,15], the interplanar distances of BOH-Zn*R* are expected to decrease due to substitution of Zn^{2+} for Bi^{3+}. Therefore the results demonstrate that the Zn^{2+} ions have incorporated into the crystal lattice of $Bi(OH)_3$ and substituted for the fractional Bi^{3+} ions. According to the Scherrer equation: $D = k\lambda/(\beta\cos\theta)$, where κ is a constant related to the crystallite shape, λ is the X-ray wavelength, and θ is the diffraction angle. The full width at half maximum (β) was obtained by fitting the diffraction peaks at 23.9° applying the Gaussian function. The mean crystallite size (D) of 19.2, 17.6, 16.9, 15.8, 13.9 nm correspond to the samples BOH and BOH-Zn*R* (R = 0.01, 0.02, 0.03 and 0.04), respectively. It displays that the mean crystallite size reduces due to Zn doping.

3.2. Morphology analysis

The SEM images of the samples BOH and BOH-Zn*R* are shown in Fig. 2. It can be seen from Fig. 2a that BOH consists of interconnected nanosheets with a thickness of less than 20 nm, which are consistent with the previously reported data [6]. From Figs. 2b–e, the samples are composed of face-to-face closely accumulated nanosheets. And size of the sheets is smaller than that of the BOH, which agrees with the results of XRD. The EDS analysis was utilized to determine the element composition of the samples. Taking the BOH-Zn0.02 as an example, as shown in Fig. 2f, the obvious signals of Bi and O and Zn elements was observed, which prove the coexistence of Zn and Bi and O elements in the final products. The Zn/Bi molar ratio is 0.0183, which is close to the theoretical value in the experiment.

The TEM image of the sample BOH-Zn0.02 is shown in Fig. 3. It can be seen that the sample consists of thin nanosheets. Through further observation, we can find some white dots adhered to the surface of the nanosheets, it was speculated that white dots may be bismuth oxide. Bismuth hydroxide is not very stable in the synthesis process and a minute quantity of the particles could be decomposed into bismuth oxide. However, the bismuth oxide content is so low that it is not be observed on the XRD patterns. Fig. 3b shows the high evolution image of the sample BOH-Zn0.02. It is clear that the lattice spacing of 0.232 nm corresponds to the (121) planes of Bi_2O_3. It demonstrates that the little Bi_2O_3 crystals distribute on the interface of $Bi(OH)_3$ nanosheets.

3.3. Chemical states analysis

In order to determine the chemical state of surface elements present in the samples, the samples BOH-ZnR with different R values were investigated by XPS. The results are shown in Fig. 4. The XPS survey spectra of all the samples show Bi, O, C elements peaks, similar to the sample BOH-Zn0.02 (Fig. 4a). Among them, C peaks have the source from the contamination carbon in the atmosphere. But no Zn element peaks could be found, which is due to Zn element with low concentration. The high-resolution XPS spectra of Bi 4f and O 1s are shown in Figs. 4b and c. Clearly, the peaks at ca. 164.8 and 159.5 eV can be assigned to Bi 4f 7/2 and Bi 4f 5/2, respectively, which were assigned to the Bi–O bonds [29,30]. The O1s spectra are fitted into the two peaks

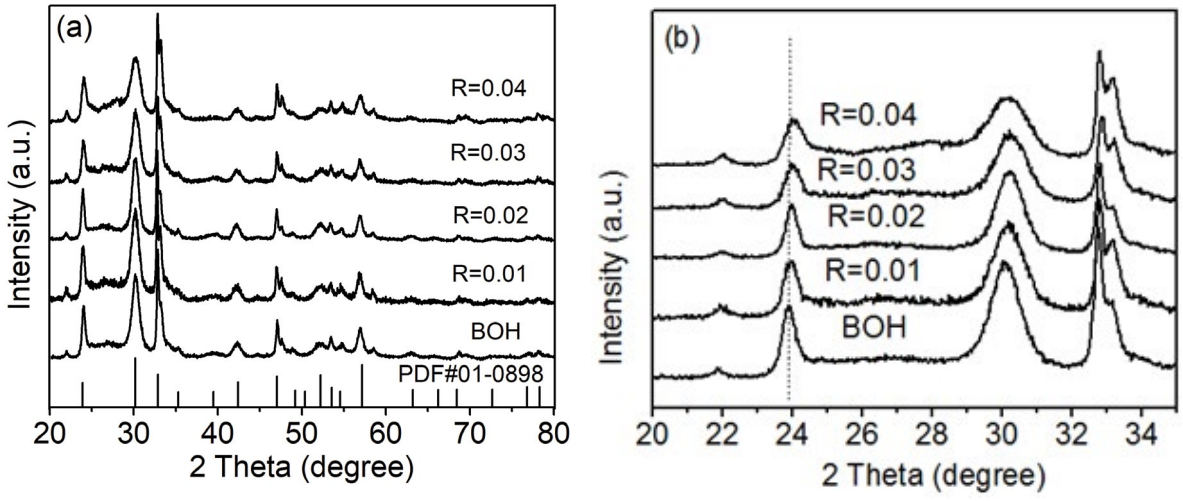

Fig. 1. (a) XRD diffraction patterns and (b) enlargement in the range of 20°–35°of the BOH and BOH-Zn*R* (R = 0.01, 0.02, 0.03 and 0.04).

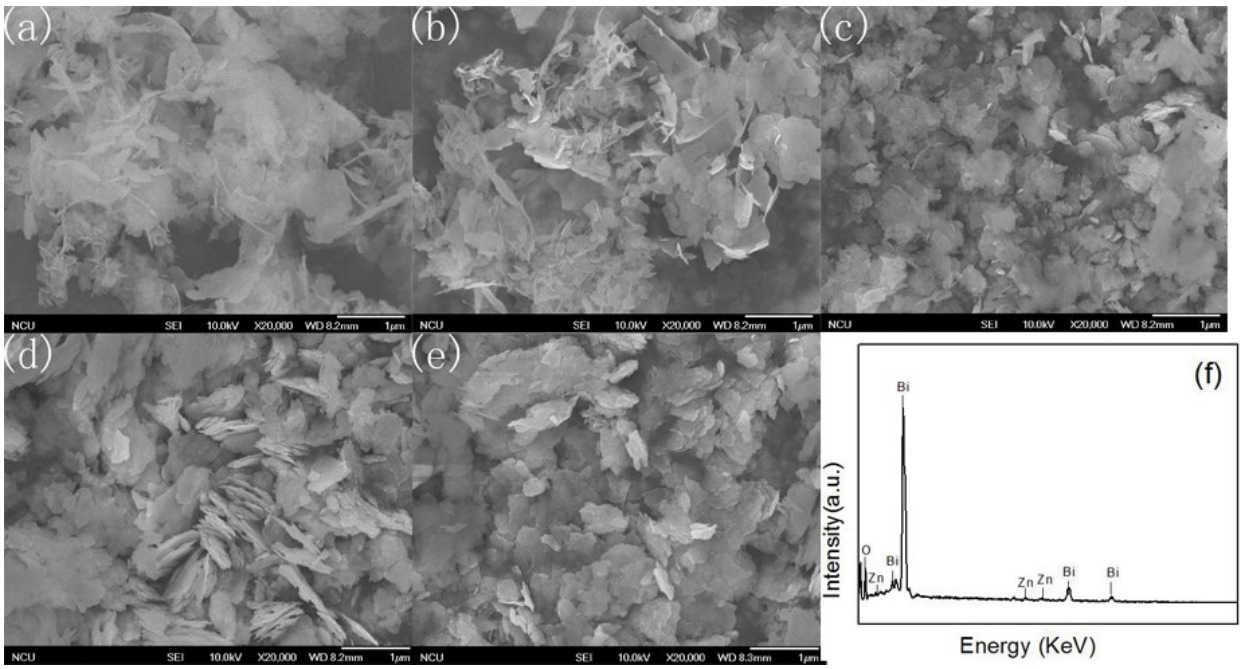

Fig. 2. SEM images of the obtained samples (a) BOH, (b) BOH-Zn0.01, (c) BOH-Zn0.02, (d) BOH-Zn0.03, (e) BOH-Zn0.04, and (f) EDS of the BOH-Zn0.02.

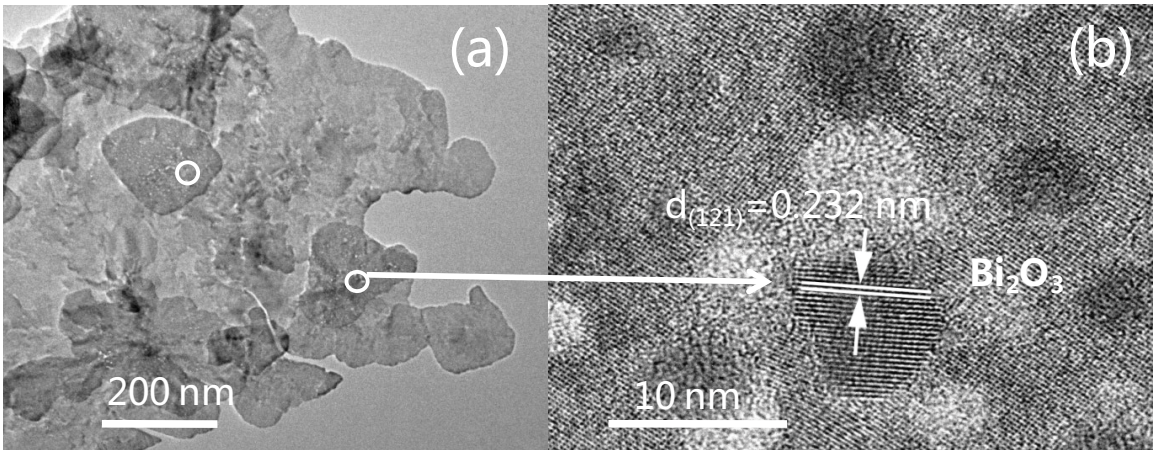

Fig. 3. TEM (a) and HRTEM image (b) of the sample BOH-Zn0.02.

at ca. 530.2 and 531.3 eV. The high binding energy (531.3 eV) is usually attributed to the chemisorbed or dissociated oxygen on the particles or OH species of hydroxides. The low binding energy (530.2 eV) is assigned to lattice oxygen of metal oxide [31]. It can be found from Figs. 4b and c that the binding energies of Bi 4f and O 1s both shift to lower binding energy with increase of the Zn content. It attributes to that the redundant electrons have been formed after Zn^{2+} ions replace Bi^{3+} ions, and the repulsive interaction leads to increase of the kinetic energy and decrease of the binding energies of photo electrons. The Zn 2p core level spectrum of the sample BOH-Zn0.02 is shown in Fig. 4d. The Zn 2p1 and Zn 2p3 spin-orbital photo electrons are located at binding energies of 1,044.8 and 1,021.9 eV, respectively, indicating that the existence of Zn^{2+} on the surface of the sample [32]. According to the XPS analysis, the Zn/Bi molar ratio is about 2.4, which is beyond the error correction of the theoretical value 2.0. It further indicates that the much more Zn ions are just doped on the surface of the samples.

3.4. Optical properties

The UV–Vis diffuse reflectance spectra of the obtained samples are shown in Fig. 5. It can be seen that all the samples almost have the same absorption edges, and the band gaps of BOH-Zn*R* samples have no significant change (Fig. 5a). The band gaps of semiconductors can be calculated according to the following Eq. (2): $(\alpha E_{photon}) = A(E_{photon}-E_g)^{n/2}$, where α, E_{photon}, A and n are the absorption coefficient, the photo energy, constant and an integer, respectively. The n is

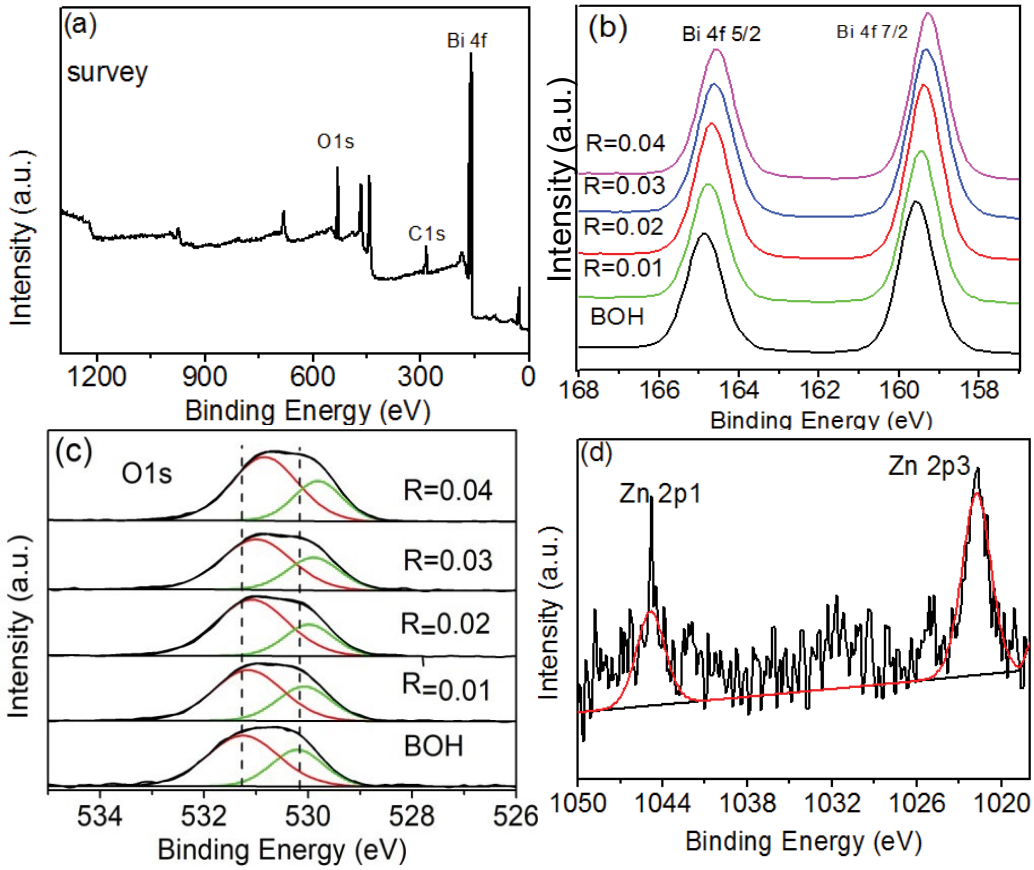

Fig. 4. XPS spectra of the samples. (a) Survey of the BOH-Zn0.02, (b, c) the high-resolution XPS spectra of Bi 4f and O 1s of BOH and BOH-Zn*R* (*R* = 0.01, 0.02, 0.03 and 0.04), respectively, (d) the high-resolution XPS spectra of Zn 2p of BOH-Zn0.02.

equal to 1 for an indirect band gap, and it is 4 for a direct band gap. According to this equation, the value of the band gap of the samples was about 3.22 eV. It is interesting that an obvious absorption tailing to about 600 nm of all the samples is observed. The absorption tailing is guessed to be caused by the BiO_X on the surface of the samples [33].

3.5. Photocatalytic activity

The photocatalytic performances of the obtained samples were investigated by the degradation of RhB under visible light irradiation ($\lambda \geq 420$ nm). Fig. 6a shows the absorption peaks intensities of RhB solution changed as function of irradiation time in the presence of BOH-Zn0.02. It can be seen the absorbance of RhB decreased gradually with the increasing irradiation time, and 85.0% RhB was degraded after 120 min. No new absorption bands and negligible hypsochromic shift is observed, implying that the absence of N-de-ethylation of RhB [34]. It indicates that the sample BOH-Zn0.02 shows excellent photocatalytic activity under visible light irradiation.

Fig. 6b shows the variations of RhB concentration (C/C_0) vs. irradiation time over the obtained samples. The adsorption rates of the as-prepared samples are 28.9%, 41.8%, 44.1%, 34.7% and 33.5% for BOH and BOH-Zn*R* (*R* = 0.01, 0.02, 0.03 and 0.04), respectively. It can be seen that BOH is the catalyst with good adsorption ability and Zn doping can further improve the adsorption capability of the catalyst. After visible light irradiation for 120 min, about 45.6% RhB was degraded by the BOH. Compared with the BOH, all the BOH-Zn*R* catalysts show higher photocatalytic efficiency. The optimum Zn/Bi molar ratio for the photocatalytic degradation of RhB is 0.02, while further increase of Zn-doping concentration led to a little decrease of photocatalytic activity. Fig. 6c shows a linear relationship between $\ln(C_0/C)$ and irradiation time t (min) of the obtained samples. The photocatalytic degradation of RhB follows pseudo-first-order kinetics,that is, $\ln(C/C_0 = kt)$ where k is the kinetic constant (min^{-1}). The kinetic constants of the samples are showed in Fig. 6d. It can be seen the k values increase and reach to the largest value (0.01093) for the BOH-Zn0.02, which was as high as about five times as that of BOH, then decrease as the Zn doping concentration increases. The results further confirm that the Zn doping plays an important role on the improvement of photocatalytic activity of the samples.

3.6. Possible photocatalytic mechanism

3.6.1. Active species

The trapping experiments were carried out to evaluate the role of the active species in the photodegradation process.

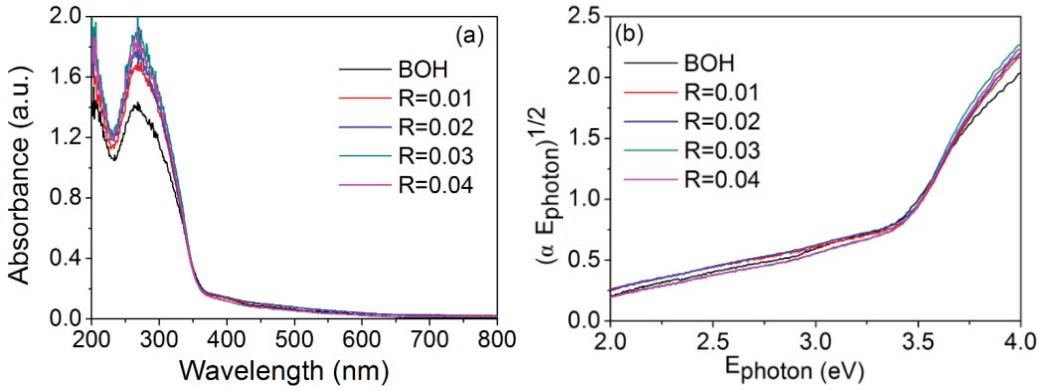

Fig. 5. (a) UV–Vis diffuse reflectance spectra, (b) plots of $(\alpha \cdot E_{photon})^{1/2}$ vs. E_{photon} curves of the BOH and BOH-Zn*R* (*R* = 0.01, 0.02, 0.03 and 0.04).

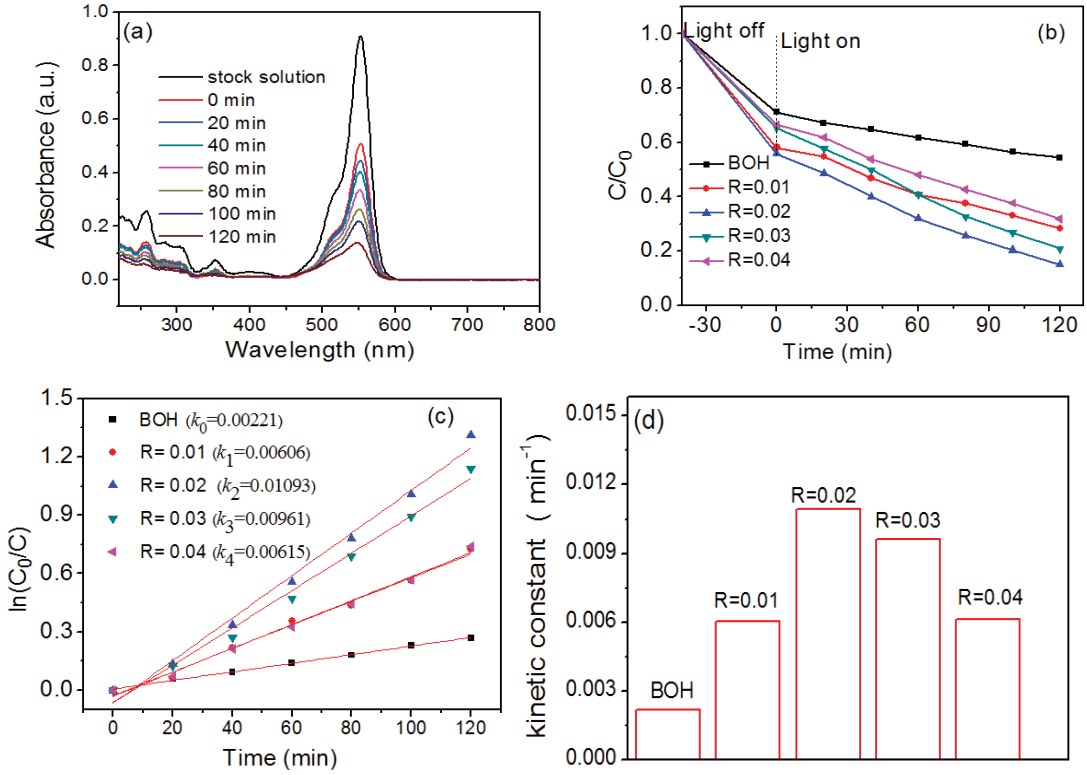

Fig. 6. (a) Temporal UV–Vis absorption spectral changes of RhB aqueous solution as a function of irradiation time in the presence of the sample BOH-Zn0.02 (0 min denoted as adsorption–desorption equilibrium and light on), (b) the photocatalytic activity, (c) plots of ln (C_0/C) vs. irradiation time, and (d) the kinetic constants of the BOH and BOH-Zn*R* (*R* = 0.01, 0.02, 0.03 and 0.04).

According to Fig. 7a, after adding 1 mmol L^{-1} IPA into photocatalytic reaction system, the degradation efficiency for RhB was reduced by ca. 9.0% compared with no scavenger. It indicates that •OH can be produced and plays some roles in the photodegradation process. When adding 1 mmol L^{-1} TEOA into the reaction system, the photocatalytic degradation of RhB was fully suppressed. It indicates that holes play a key role in the photocatalytic process. Fig. 7b shows the UV–Vis absorption spectra of NBT in the suspension of BOH-Zn0.02 under visible light irradiation ($\lambda \geq 420$ nm). The maximum absorbance has no obvious decline as the irradiation time increases, indicating without formation of $O_2^{\bullet-}$ in the photocatalytic process. Therefore, it can be concluded that the degradation of RhB was mainly due to the reaction with the photogenerated holes directly.

3.6.2. Band gap structures and the possible degradation mechanism

Usually, photocatalytic efficiency depends on the transformation and recombination rate of electron–hole pairs. The transfer rate of electron–hole pairs is related with

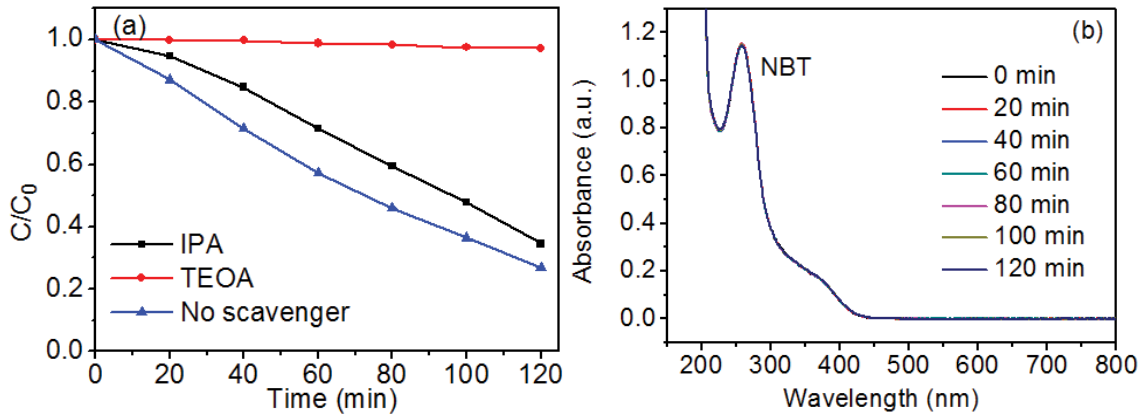

Fig. 7. (a) Effect of IPA and TEOA on the photocatalytic activity of BOH-0.02 for degradation of RhB. and (b) UV–Vis absorption spectra of NBT in the suspension of BOH-Zn0.02 under visible light irradiation ($\lambda \geq 420$ nm).

interface and energy band structure of the semiconductor [36]. In other word, the conduction and valence band positions determine the reducing and oxidation capability of catalysts. As for Bi-base semiconductors, the conduction band is composed of Bi 6p orbits. And the Bi 6s and O 2p levels can form a preferable hybridized valence band [37,38]. And these band structures are beneficial to the potential requirement of organic oxidation. We determined the valence band (VB) XPS spectra of the prepared samples. And we found that an interesting thing occurred. Zn doping could change the valence band top position of the samples. The results are shown in Fig. 8. The VB top estimated from the VB-XPS was 2.43, 2.25, 2.12, 2.23 and 2.34 eV for the BOH and BOH-Zn*R* (*R* = 0.01, 0.02, 0.03 and 0.04), respectively. Compared with BOH, the VB position of the BOH-Zn0.02 was upward shifts by 0.31 eV. According to the DRS analysis, the band gaps of all the obtained samples were 3.22 eV. Based on the formula: $E_{CB} = E_{VB} - E_g$, the conduction band (CB) minimum values of the BOH and BOH-Zn*R* (*R* = 0.01, 0.02, 0.03 and 0.04) occur at about –0.79, –0.97, –1.10, –0.99 and –0.88 eV, respectively.

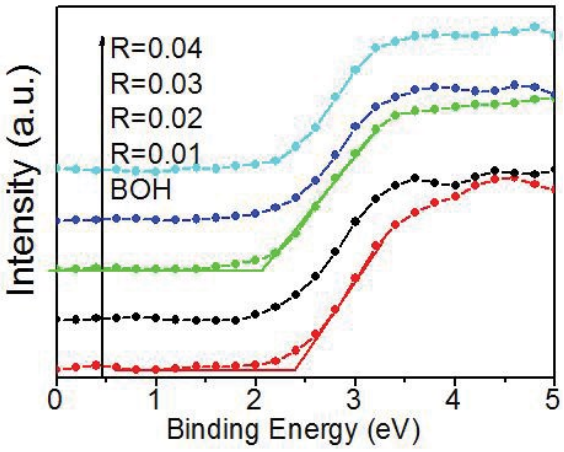

Fig. 8. Valence band XPS spectra of the BOH and BOH-Zn*R* (*R* = 0.01, 0.02, 0.03, 0.04).

To investigate the adsorption and interaction between the BOH-Zn0.02 and RhB, we determined the chemical states of the Bi element on the surface of BOH-Zn0.02 after adsorption of RhB. The results are shown in Fig. 9. The Bi 4f spectra were fitted into the two groups of peaks, which were located at 159.5, 165.0 eV and 161.0, 166.4 eV. The first group of peaks can be assigned to the Bi–O bonds [29,30]. Compared with the Bi–O bands, the second group of peaks was shifted to the higher binding energy. We speculate the higher Bi 4f binding energies are due to the chemical interaction between Bi^{3+} and the adsorbed RhB species on the surface of BOH-Zn0.02. The chemical interaction between Bi^{3+} and RhB can effectively reduce the contact energy barrier [39], which is advantageous to the transformation of electrons from the RhB to the BOH-Zn0.02 during the photocatalytic degradation. Since the upwards of energy band structures, direction of the electric field is from the bulk to the surface of the catalysts. It is in favor of the adsorption of the electron acceptor molecular (RhB), which is demonstrated by the excellent adsorption property of the BOH-Zn0.02. Meanwhile, direction of the electric field from the bulk to interface of catalysts accelerates the enrichment of holes on the interface. The photoreaction with holes as reactive species easily takes place, which was proved by the previous trapping experiments.

And we further verified the interaction between Bi ions and RhB species by FTIR spectra. The results are shown in Fig. 10. Preparation procedure of the sample BOH-Zn0.02 adsorbing RhB is as follows: 0.10 g of the sample BOH-Zn0.02 was added into the 250 mL of RhB solution with the concentration of 10 mg L^{-1}. And the suspension was ultrasounded for 10 min and stirred for 40 min in the dark in order to reach the adsorption–desorption equilibrium, then filtered and dried at 60°C in air. For the sample BOH-Zn0.02 (Fig. 10a), the IR bands at 1,604 and 1,385 cm^{-1} are assigned as antisymmetric and symmetric ν ($-CO^{2-}$) modes, respectively, of carboxylate [40], which were applied during the preparation of the catalysts. All peaks below 1,000 cm^{-1} are typical of various vibration modes of M–O and M–OH where M signifies the metal (in this case Bi). Broad band at 3,400 cm^{-1} are linked to the OH vibrations of the water molecules and the hydrogen atoms bound to the OH groups in the metal hydroxide [40].

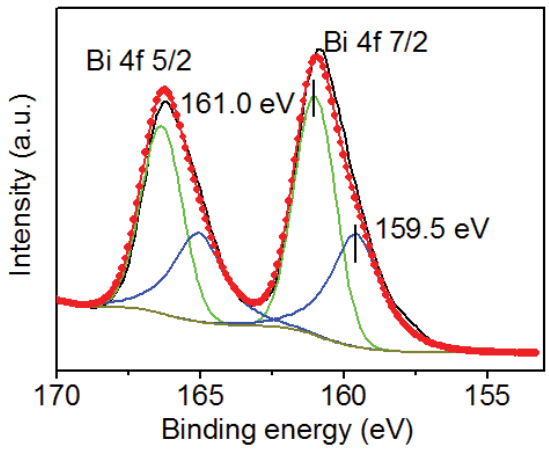

Fig. 9. XPS spectra of the Bi 4f of the sample BOH-Zn0.02 after adsorption of RhB.

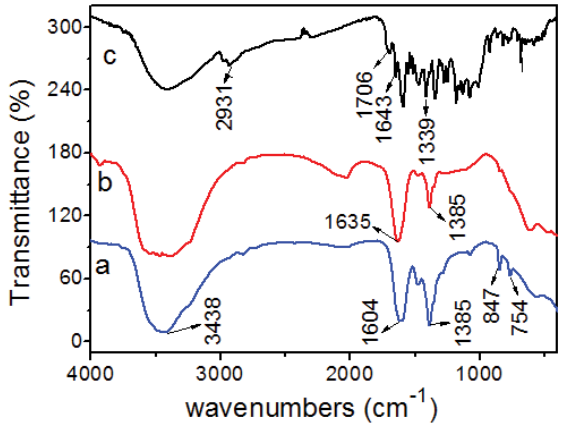

Fig. 10. FTIR spectra of (a) BOH-Zn0.02, (b) RhB molecules adsorbed onto BOH-Zn0.02, and (c) RhB powder.

RhB possesses inorganic functional groups (deprotonated carboxylic acid group and two amino groups) possibly interact with the interface of photocatalyst through coordination with metal ions and electrostatic attraction and H-bonding. For the pure RhB (Fig. 10c), the stretching vibration of the carboxyl group is located at 1,706 cm^{-1}. The N-aryl bond vibrations are located at the 1,339 cm^{-1} band. The C=N bond is located at 1,643 cm^{-1}. The OH stretching vibration of the adsorbed water was at ca. 3,418 cm^{-1} [41].

After the sample BOH-Zn0.02 adsorbing RhB (Fig. 10b), the stretching vibration band of the carboxylic group (1,706 cm^{-1}) over the sample was disappeared. Meanwhile, the stretch at 1,604 cm^{-1} shifts to ca. 1,635 cm^{-1} and is strengthened and broadened, and the vibration at 1,385 cm^{-1} is much weaker compared with the band of the carboxylate in the BOH. This splitting vibration was also observed in the RhB coordination with TiO_2 [42,43]. Generally, the frequency difference (Δ) between the antisymmetric and symmetric stretching vibration of carboxyl group in various chemical environment is in the order of -(monodentate) > -(ionic) -(bridging) > -(bidentate)- [44–46]. In our work, the Δ value (250 cm^{-1}) of carboxyl group illustrates that carboxyl group links with the Bi^{3+} by monodentate coordination. In other words, it is likely that Bi ions further coordinating with carboxyl groups in the RhB species leads to increased vibration dipole moments of carboxyl groups, corresponding to the vibration transmittance peak intensity undergoing changes.

We estimated the separation of photogenerated electron and hole pairs of the samples by the PL spectra. Fig. 11a shows the PL spectra of the as-prepared samples using an excitation wavelength of 360 nm. The two PL emission peaks at 404 nm (3.07 eV) and 472 nm (2.62 eV) were found. The lower PL photon energy, compared with the bandgap energy of the obtained samples (3.22 eV) indicates that the electron–hole pairs may recombine via the trap states. Additionally, it can be seen that all the Zn-doped BOH samples show lower PL intensities than the bare BOH, proving that Zn doping can inhibit the recombination of electron–hole pairs. PL results indicate that upward of energy band can improve the transfer rate of carriers and decrease their recombination.

The photocatalytic activity of catalysts was influenced by several factors such as morphology, particle size, specific surface area, optical absorption ability and energy band structure [47,48]. We determined the specific surface area of the obtained samples. The specific surface areas of the BOH and BOH-Zn (R = 0.01, 0.02, 0.03 and 0.04) were estimated to be 27.5, 26.8, 26.1, 25.7, 25.5 $m^2 g^{-1}$, respectively. All of samples had similar specific surface areas. Then we determined the N_2 adsorption–desorption isotherms and pore volume and pore diameter distribution of BOH and BOH-Zn0.02 (Fig. 11b). The results displayed the type IV isotherms with obvious hysteresis (P/P_0 = 0.4–1.0) between the adsorption and desorption branches, indicating the presence of mesopores. The inset graphs of Fig. 11b show the pore volume and pore diameter distribution of BOH and BOH-Zn0.02 were similar. Moreover, the light absorption curves of the samples are almost consistent, which indicates that the specific surface area and light absorption property are not the main effecting factor in this system.

Then what results in the enhancement of photocatalytic performance of the Zn dopant $Bi(OH)_3$ under visible light illumination?

According to the discussion above, the energy band bending of the products is possibly the key factor of improvement of photoactivity. Band bending can influence the photoreaction process by the following way [21]. (1) Thermal adsorption or desorption of the objective species on the surface of semiconductors, which were proved by the results of adsorption experiment of RhB on the products. (2) Modulating photogeneration carriers recombination and transfer process between the semiconductors and adsorbates.

The potential of LUMO and HOMO levels of RhB are –1.42 and 0.95 eV, respectively, which match very well with λ_{max} of 553 nm [49,50]. Since the potential of LUMO of RhB is more negative than position of conduction band of the BOH-Zn0.02. So the photoexcited electrons from RhB can transfer to conduction band of the BOH-Zn0.02. Based on the above analysis and discussion, a plausible photocatalytic process was proposed, as illustrated in Fig. 12. When the adsorbed RhB species are excited by visible light, the photogenerated electrons are injected into the conduction band

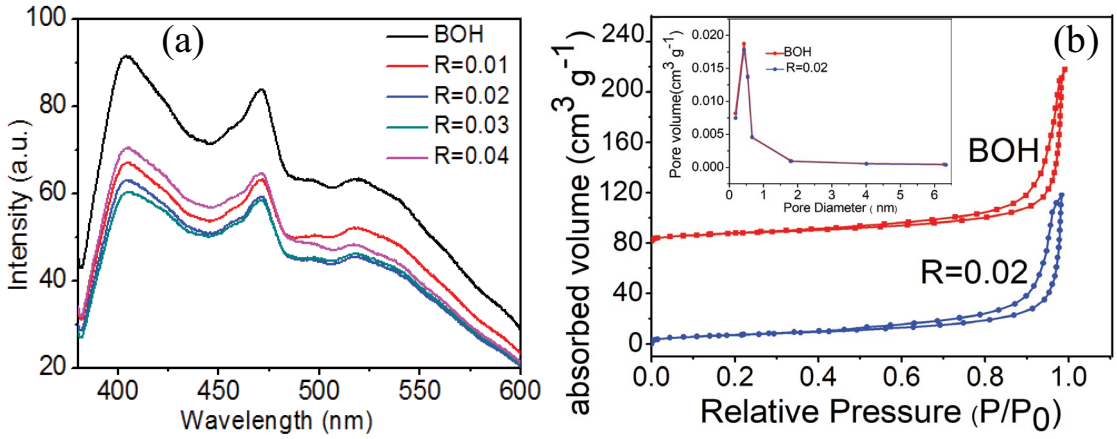

Fig. 11. (a) PL spectra of the BOH and BOH-Zn samples with different *R* values and (b) N_2 adsorption–desorption isotherms of BOH and BOH-Zn0.02 (inset is the pore volume and average pores diameter distribution of BOH and BOH-Zn0.02).

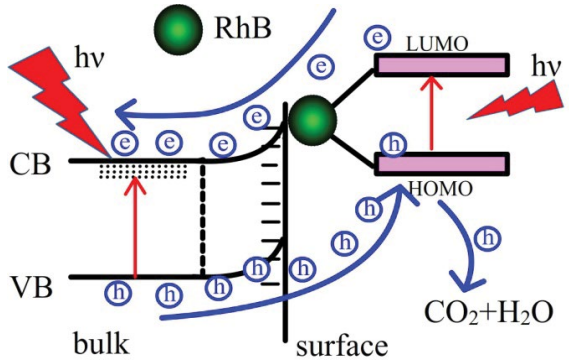

Fig. 12. Photogenerated carriers transfer process on the surface of the BOH-Zn0.02 absorbing RhB by visible light illumination ($\lambda \geq 420$ nm).

of the BOH-Zn0.02. Meanwhile, the BOH-Zn0.02 is irradiated by visible light and the photogenerated electrons on the surface easily transfer into the bulk of the BOH-Zn0.02 due to upward band bending. However the photogenerated holes could transport the HOMO level of RhB since the BOH-Zn0.02 has more positive potential level. So photogenerated electrons and holes can be effectively separated. Much more holes can be applied for degradation of RhB.

4. Conclusions

In summary, BOH-Zn with different contents of zinc was successfully synthesized via a solvothermal method. The Zn doping did not change the BET surface area and the light absorption property of BOH. However, Zn dopant could induce the upward band bending. Accordingly, Zn doping could highly improve the photocatalytic activity for degradation of Rhodamine B (RhB) under visible light irradiation ($\lambda \geq 420$ nm). The sample with the Zn/Bi molar ratio of 0.02 showed the highest photocatalytic activities, and its apparent rate constant was five times higher than the bare $Bi(OH)_3$. The photogenerated holes played a key role in this photocatalytic reaction process. The high photocatalytic activity could be attributed to high adsorption capability and photogenerated carriers rapidly transfer between the Zn-doped $Bi(OH)_3$ and RhB species due to upward band bending.

Acknowledgements

The financial support of this study from the National Natural Science Foundation of China (21563020, 21465017) is gratefully acknowledged.

References

[1] I.K. Konstantinou, T.A. Albanis, TiO_2-assisted photocatalytic degradation of azo dyes in aqueous solution: kinetic and mechanistic investigations: a review, Appl. Catal., B, 491 (2004) 1–14.
[2] C.Q. Xu, H.H. Wu, F.L. Gu, Efficient adsorption and photocatalytic degradation of rhodamine B under visible light irradiation over BiOBr/montmorillonite composites, J. Hazard. Mater., 275 (2014) 185–192.
[3] Y. Gu, Z.D. Xu, L. Guo, Y.Q. Wan, ZnO nanoplate-induced phase transformation synthesis of the composite $ZnS/In(OH)_3/In_2S_3$ with enhanced visible-light photodegradation activity of pollutants, CrystEngComm, 16 (2014) 10997–11006.
[4] M.L. Guan, C. Xiao, J. Zhang, S.J. Fan, R. An, Q.M. Cheng, J.F. Xie, M. Zhou, B.J. Ye, Y. Xie, Vacancy associates promoting solar-driven photocatalytic activity of ultrathin bismuth oxychloride nanosheets, J. Am. Chem. Soc., 135 (2013) 10411–10417.
[5] X.X. Zeng, X.F. Gong, Y.Q. Wan, Z.D. Xu, Additive dependent synthesis of bismuth oxybromide composites for photocatalytic removal of the antibacterial agent ciprofloxacin and mechanism insight, RSC Adv., 7 (2017) 36269–36278.
[6] W. Zhang, X.X. Huang, Y.Y. Tan, Y.L. Gao, J.X. Wu, J.B. Hu, A. Stein, B. Tang, A facile approach to prepare $Bi(OH)_3$ nanoflakes as high-performance pseudocapacitor materials, New J. Chem., 39 (2015) 5927–5930.
[7] K.V. Terebilenko, K.L. Bychkov, V.N. Baumer, N.S. Slobodyanik, M.V. Pavliuk, A. Thapper, I.I. Tokmenko, I.M. Nasieka, V.V. Strelchuk, Structural transformation of $Bi_{1-x}/3V_{1-x}Mo_xO_4$ solid solutions for light-driven water oxidationt, Dalton Trans., 45 (2016) 3895–3904.
[8] X. Zhang, X. Quan, S. Chen, Y. Zhang, Effect of Si doping on photoelectrocatalytic decomposition of phenol of $BiVO_4$ film under visible light, J. Hazard. Mater., 177 (2010) 914–917.
[9] S. Kohtani, M. Tomohiro, K. Tokumura, R. Nakagaki, Photooxidation reactions of polycyclic aromatic hydrocarbons over

pure and Ag-loaded $BiVO_4$ photocatalysts, Appl. Catal., B, 58 (2005) 265–272.
[10] W. Yao, H. Iwai, J. Ye, Effects of molybdenum substitution on the photocatalytic behavior of $BiVO_4$, Dalton Trans., 11 (2008) 1426–1430.
[11] H. Jiang, H. Endo, H. Natori, M. Nagai, K. Kobayashi, Fabrication and efficient photocatalytic degradation of methylene blue over CuO/$BiVO_4$ composite under visible-light irradiation, Mater. Res. Bull., 44 (2009) 700–706.
[12] M. Long, W.M. Cai, J. Cai, B.X. Zhou, X.Y. Chai, Y.H. Wu, Efficient photocatalytic degradation of phenol over Co_3O_4/$BiVO_4$ composite under visible light irradiation, J. Phys. Chem. B, 110 (2006) 20211–20216.
[13] B. Pare, B. Sarwan, S.B. Jonnalagadda, Photocatalytic mineralization study of malachite green on the surface of Mn-doped BiOCl activated by visible light under ambient condition, Appl. Surf, Sci., 258 (2011) 247–253.
[14] W.T. Li, W.Z. Huang, H. Zhou, H.Y. Yin, Y.F. Zheng, X.C. Song, Synthesis of Zn^{2+} doped BiOCl hierarchical nanostructures and their exceptional visible light photocatalytic properties, J. Alloys Compd., 638 (2015) 148–154.
[15] X.C. Song, Y.F. Zheng, H.Y. Yin, J.N. Liu, X.D. Ruan, The solvothermal synthesis and enhanced photocatalytic activity of Zn^{2+} doped BiOBr hierarchical nanostructures, New J. Chem., 40 (2016) 130–135.
[16] L. Bi, D. Xu, L. Zhang, Y. Lin, D. Wang, T. Xie, Metal Ni-loaded g-C_3N_4 for enhanced photocatalytic H_2 evolution activity: the change in surface band bending. Phys. Chem. Chem. Phys., 17 (2015) 29899–29905
[17] C.G. Zhou, J.K. Zhou, L. Lu, J.J. Wang, Z. Shi, B. Wang, L. Pei, S.C. Yan, Z.T. Yu, Z.G. Zou, Surface electric field driven directional charge separation on Ta_3N_5 cuboids enhancing photocatalytic solar energy conversion. Appl. Catal., B, 237 (2018) 742–752.
[18] E. Lira, S. Wendt, P.P. Huo, J.Q. Hansen, R. Streber, S. Porsgaard, Y.Y. Wei, R. Bechstein, E. Lægsgaard, F. Besenbacher, The importance of Bulk Ti^{3+} Defects in the Oxygen Chemistry on Titania Surfaces, J. Am. Chem. Soc., 13 (2011) 6529–6532.
[19] Y.J. Lin, Y.L. Chu, Effect of reactive ion etching-induced defects on the surface band bending of heavily Mg-doped p-type GaN, J. Appl. Phys., 97 (2005) 1–8.
[20] M. Hamadanian, M. Shamshiri, V. Jabbari, Novel high potential visible-light-active photocatalyst of CNT/Mo, S-codoped TiO_2 hetero-nanostructure, Appl. Surf. Sci., 317 (2014) 302–311
[21] Z. Zhang, J.Y. Jr, Band Bending in Semiconductors: Chemical and Physical Consequences at Surfaces and Interfaces, Chem. Rev., 112 (2012) 5520−5551.
[22] Y.X. Li, Y.L. Hou, Q.Y. Fu, S.Q. Peng, Y.H. Hu, Oriented growth o f $ZnIn_2S_4$/$In(OH)_3$ heterojunction by a facile hydrothermal transformation for efficient photocatalytic H_2 production, Appl. Catal., B, 206 (2017) 726–733.
[23] G.Q. Li, N. Yang, W.W. Wang, W.F. Zhang, Band structure and photoelectrochemical behavior of $AgNbO_3$–$NaNbO_3$ solid solution photoelectrodes, Electrochim. Acta, 55 (2010) 7235–7239.
[24] S.X. Ouyang, H. Tong, N. Umezawa, J.Y. Cao, P. Li, Y.P. Bi, Y.J. Zhang, J.H. Ye, Surface-Alkalinization-Induced Enhancement of Photocatalytic H_2 Evolution over $SrTiO_3$-Based Photocatalysts, J. Am. Chem. Soc., 134 (2012) 1974–1977.
[25] Y.Q. Wang, H. Cheng, Y.Z. Hao, J.M. Ma, W.H. Li, S.M. Cai, Photoelectrochemical properties of metal-ion-doped TiO_2 nanocrystalline electrodes, Thin Solid Films, 349 (1999) 120–125.
[26] A.W. Xu, Y.Gao, H.Q. Liu, The preparation, characterization, and their photocatalytic activities of rare-earth-doped TiO_2 nanoparticles, J. Catal., 207 (2002) 151–157.
[27] W.Y. Choi, A. Termin, M.R. Hoffmann, The role of metal-ion dopants in quantum-sized TiO_2-correlation between photoreactivity and charge-carrier recombination dynamics, J. Phys. Chem., 98 (1994) 13669–13769.
[28] K. Nagaveni, M.S. Hegde, G. Madras, Structure and photocatalytic activity of $Ti_{1-x}M_xO_2$ +/-delta (M = W, V, Ce, Zr, Fe, and Cu) synthesized by solution combustion method, J. Phys. Chem. B, 108 (2004) 20204–20212.
[29] X.X. Zeng, X.F. Gong, Y.Q. Wan, R.Y. He, Z.D. Xu, Formation of Oxygen Vacancies on the {010} Facets of BiOCl and Visible Light Activity for Degradation of Ciprofloxacin, Chem. Res. Chin. Univ., 34 (2018) 711–718.
[30] X.W. Liu, H.Q. Cao, J.F. Yin, Generation and Photocatalytic Activities of Bi@Bi_2O_3 Microspheres, Nano Res, 4 (2011) 470–482.
[31] L. Pan, T. Muhammad, L. Ma, Z.F. Huang, S. Wanga, L. Wanga, J.J. Zoua, X.W. Zhang. MOF-derived C-doped ZnO prepared via a two-step calcination for efficient photocatalysis[J], Appl. Catal., B, 189 (2004) 181–191.
[32] Y.H. Zheng, L.R. Zheng, Y.Y. Zhan, X.Y. Lin, Q. Zheng, K.M. Wei, Ag/ZnO heterostructure nanocrystals: synthesis, characterization, and photocatalysis, Inorg. Chem., 46 (2007) 6980–6986.
[33] W.J. Fang, Z. Jiang, L. Yu, H. Liu, W. Feng, S. Guan, C. Terashima, A. Fujishima, Novel dodecahedron $BiVO_4$:YVO_4 solid solution with enhanced charge separation on adjacent exposed facets for highly efficient overall water splitting, J. Catal., 35 (2017) 155–159.
[34] T. Watanabe, T. Takizawa, K. Honda, Photocatalysis through excitation of adsorbates. 1. Highly efficient N-deethylation of rhodamine B adsorbed to cadmium sulfide, J. Phys. Chem., 81 (1977) 1845–1851.
[35] N. Kislov, J. Lahiri, H. Verma, D.Y. Goswami, E. Stefanakos, M. Batzill. Photocatalytic degradation of Methyl Orange over single crystalline ZnO: orientation dependence of photoactivity and photostability of ZnO, Langmuir, 25 (2009) 3310–3315.
[36] M. Sathish, B. Viswanathan, R.P. Viswanath, C.S. Gopinath, Synthesis, characterization, electronic structure, and photocatalytic activity of nitrogen-doped TiO_2 nanocatalyst, Chem. Mater., 17 (2005) 6349–6353.
[37] A. Kudo, K. Omori, H. Kato, A novel aqueous process for preparation of crystal form-controlled and highly crystalline $BiVO_4$ powder from layered vanadates at room temperature and its photocatalytic and photophysical properties, J. Am. Chem. Soc., 121 (1999) 11459–11467.
[38] M. Wiegel, W. Middel, G. Blasse, Influence of Ns(2) ions on the luminescence of niobates and tantalates, J. Mater. Chem., 5 (1995) 981–983.
[39] J.L. Hu, W.J. Fan, W.Q. Ye, C.J. Huang, X.Q. Qiu, Insights into the photosensitivity activity of BiOCl under visible light irradiation, Appl. Catal., B, 158–159 (2014) 182–189.
[40] Z.A. Hu, Y.L. Xie, Y.X. Wang, L.J. Xie, G.R. Fu, X.Q. Jin, Z.Y. Zhang, Y.Y. Yang, H.Y. Wu, Synthesis of alpha-Cobalt hydroxides with different intercalated anions and effects of intercalated anions on their morphology, basal plane spacing, and capacitive property, J. Phys. Chem. C, 113 (2009) 12502–12508.
[41] Y.X. Pan, D.H. Mei, C.J. Liu, Q.F. Ge, Hydrogen adsorption on Ga_2O_3 surface: a combined experimental and computational study, J. Phys. Chem. C, 115 (2011) 10140–10146.
[42] A. Couzis, E. Gulari, Adsorption of sodium laurate from its aqueous solution onto an alumina surface. A dynamic study of the surface-surfactant interaction using attenuated total reflection Fourier transform infrared spectroscopy, Langmuir, 9 (1993) 3414–3421.
[43] D. Zhao, C.C. Chen, Y.F. Wang, W.H. Ma, J.C. Zhao, T.J. Rajh, L. Zhang, Enhanced photocatalytic degradation of dye pollutants under visible irradiation on Al(III)-modified TiO_2: structure, interaction, and interfacial electron transfer, Environ. Sci. Technol., 42 (2008) 308–314.
[44] D. Wang, L.J. Wan, C. Wang, C.L. Bai, In Situ STM Evidence for Adsorption of Rhodamine B in Solution, J. Phys. Chem. B, 106 (2002) 4223–4226.
[45] Y.X. Weng, L. Li, Y. Liu, L. Wang, G.Z. Yang, Surface-Binding Forms of carboxylic groups on nanoparticulate TiO_2 surface studied by the interface-sensitive transient triplet-state molecular probe, J. Phys. Chem. B, 107 (2003) 4356–4363.
[46] S.W. Boettcher, M.H. Bartl, J.G. Hu, G.D. Stucky, Structural Analysis of Hybrid Titania-Based Mesostructured Composites, J. Am. Chem. Soc., 127 (2005) 9721–9730.
[47] G.L. Huang, Y.F. Zhu, Synthesis and photoactivity enhancement of $ZnWO_4$ photocatalysts doped with chlorine, CrystEngComm, 14 (2012) 8076–8082.

[48] Y. Liu, Y. Lv, Y. Zhu, D. Liu, R. Zong, Y. Zhu, Fluorine mediated photocatalytic activity of $BiPO_4$, Appl. Catal., B, 147 (2014) 851–857.
[49] S. Kumar, T. Surendar, A. Baruah, V. Shanker, Synthesis of a novel and stable g-C_3N_4-Ag_3PO_4 hybrid nanocomposite photocatalyst and study of the photocatalytic activity under visible light irradiation, J. Mater. Chem. A, 1 (2013) 5333–5340.
[50] L. Pan, J. Zou, X. Liu, X. Liu, S. Wang, X. Zhang, L. Wang, Visible-light-induced photodegradation of Rhodamine B over hierarchical TiO_2: effects of storage period and water-mediated adsorption switch, Ind. Eng. Chem. Res., 51 (2012) 12782–12786.